TITLE

PDZD8 deficiency drives lipid accumulation in SNr and dopaminergic disinhibition

Running title

SNr lipid accumulation drives dopaminergic disinhibition

Authors

Tomoya Ozaki[1†], Yumi Morisugi[1†], Mei Kamino[1†], Hizuki Takahashi[1], Miki Iwata[1], Honoka Maki[1], and Michiko Shirane[1]*

[1]Department of Molecular Biology, Graduate School of Pharmaceutical Sciences, Nagoya City University, Nagoya, Aichi, Japan

***Correspondence**

Michiko Shirane, shiram@phar.nagoya-cu.ac.jp

[†]These authors have contributed equally to this work and share first authorship

Keywords: Brain, Basal ganglia, Dopamine, SNr, Lipid, PDZD8, ADHD

ABSTRACT

The basal ganglia integrate cortical inputs to regulate motor, cognitive, and emotional behaviors through precisely balanced inhibitory and excitatory circuits. The substantia nigra pars reticulata (SNr) serves as a major output nucleus exerting tonic inhibition over thalamic and midbrain targets. However, how lipid metabolic disturbances affect SNr circuitry and dopaminergic regulation remains unclear. Here, we identify a crucial role for the lipid transport protein PDZD8 in maintaining basal ganglia circuit integrity. PDZD8 deficiency leads to marked lipid and lipofuscin accumulation selectively in the SNr, accompanied by enhanced striatal inhibitory inputs and reduced SNr projections to thalamus and midbrain dopaminergic nuclei. This circuit reorganization results in functional disinhibition and hyperactivation of dopaminergic neurons, producing maladaptive reinforcement of striatal inhibition. Our previous findings revealed that PDZD8$^{-/-}$ mice exhibit hyperactivity, reduced anxiety, and impaired fear memory, behavioral phenotypes reminiscent of attention-deficit/hyperactivity disorder (ADHD). These findings demonstrate that lipid accumulation in the SNr disrupts inhibitory output and dopaminergic regulation, forming a maladaptive basal ganglia–thalamocortical loop. Our study provides the first mechanistic link between lipid metabolic dysfunction, dopaminergic disinhibition, and ADHD-like behavioral phenotypes, highlighting PDZD8 as a key regulator of metabolic–circuit coupling in the basal ganglia.

INTRODUCTION

Basal ganglia and striatonigral pathway

The basal ganglia constitute a key component of the volitional motor system and contribute to essential aspects of cognition, sensorimotor integration, emotion, and learning. Dysfunction of basal ganglia circuits is implicated in a wide range of neurological and neuropsychiatric disorders(Park et al., 2020; Foster et al., 2021; McElvain et al., 2021). Current models describe three partially segregated channels of information flow through the basal ganglia—associative, limbic, and sensorimotor—which are further refined into multiple parallel subnetworks(Alexander et al., 1986; Grillner and Robertson, 2016). The cortico–basal ganglia–thalamic network (the basal ganglia–thalamocortical circuitry) represents one of the fundamental network motifs of the brain, consisting of precisely organized and reciprocally connected nodes(Foster et al., 2021; McElvain et al., 2021). Within this loop, the striatum, pallidum, and substantia nigra integrate widespread cortical inputs. The striatonigral (direct) pathway exhibits greater convergence than the striatopallidal (indirect) pathway, yet both ultimately converge onto the same output neurons within the substantia nigra pars reticulata (SNr), emphasizing the integrative nature of SNr-mediated control (Foster et al., 2021).

SNr as a major output nucleus of basal ganglia

SNr is the principal output nucleus of the basal ganglia, composed predominantly of inhibitory GABAergic neurons that project to specific thalamic nuclei and brainstem regions(Foster et al., 2021; McElvain et al., 2021; Falasconi et al., 2025). SNr neurons exhibit high tonic firing rates that maintain downstream targets under constant inhibition, whereas transient decreases in firing rate permit movement initiation via disinhibition. Recent studies have revealed that SNr neurons display multiphasic, bidirectional firing dynamics—both decreases and increases—allowing temporally precise modulation of downstream circuits during sequential motor acts(Falasconi et al., 2025). Notably, the caudal and lateral subregions of the SNr, which receive inputs from defined striatal territories, exhibit highly organized topographic projections(Lee et al., 2020; McElvain et al., 2021). These findings suggest that SNr subcircuits play specialized roles in coordinating movement and behavioral control.

SNr dysfunction and neuropsychiatric disorders

Attention-deficit/hyperactivity disorder (ADHD) is characterized by inattention, hyperactivity, and impulsivity, and is linked to altered dopaminergic and noradrenergic signaling(Biederman, 2005; Thapar and Cooper, 2016). Reduced cortical and subcortical gamma-amino butyric acid (GABA) levels have also been reported in ADHD. Among inhibitory neurons, parvalbumin-positive (PV^+) neurons play a key role in attentional

processes and motor control, and their dysfunction has been implicated in multiple psychiatric conditions, including schizophrenia, autism spectrum disorder, and ADHD(Lewis et al., 2005; Sohal et al., 2009). PV^+ neurons in the SNr provide critical feedforward inhibition and disinhibition within basal ganglia circuits. Recent work demonstrated that loss of histamine H_2 receptor (H_2R) expression in SNr PV^+ neurons leads to diminished neuronal activity and behavioral phenotypes resembling ADHD—hyperactivity, impulsivity, and inattention(Kim et al., 2016; Rizzi and Tan, 2019; An et al., 2025). Notably, this dysfunction in SNr PV^+ neurons, but not in medial prefrontal PV^+ neurons, was associated with elevated striatal dopamine levels, implicating the SNr as a key node in the dopaminergic dysregulation underlying ADHD(An et al., 2025).

Lipid metabolism and neuronal function

Lipid accumulation has long been associated with neurodegenerative conditions such as Alzheimer's disease (AD)(Dahm, 2006; Foley, 2010). The discovery of apolipoprotein E4 (ApoE4) as the strongest genetic risk factor for AD highlighted the importance of lipid metabolism in brain health(Lambert et al., 2013). Abnormal accumulation of cholesteryl esters (CEs)—neutral lipids involved in cholesterol transport—has been observed in brains of AD patients and AD model animals(van der Kant et al., 2019; Nugent et al., 2020; Blanchard et al., 2022; Litvinchuk et al., 2024). ApoE4-containing lipoproteins tend to aggregate within lysosomes, impairing degradation and promoting lipid peroxidation and inflammation. In neurons and glia carrying ApoE4, CEs accumulate in lysosomes and transform into lipofuscin, an autofluorescent granule composed of peroxidized lipids and damaged proteins that is highly resistant to degradation(Guo et al., 2025). Excessive lipofuscin accumulation leads to lysosomal stress and chronic neuroinflammation, processes increasingly recognized as drivers of neurodegeneration(Terman and Brunk, 2004; Gray and Woulfe, 2005; Moreno-Garcia et al., 2018).

PDZD8 and lipid homeostasis in the brain

We previously identified PDZD8 as a tethering protein at intracellular membrane contact sites (MCSs) between the endoplasmic reticulum (ER) and endosomes through proteomic analysis of the protrudin complex(Shirane and Nakayama, 2006; Shirane et al., 2020). PDZD8 belongs to the tubular lipid-binding (TULIP) superfamily and contains a synaptotagmin-like mitochondrial-lipid-binding (SMP) domain that mediates lipid transfer. We demonstrated that PDZD8 facilitates cholesterol transport(Shirane et al., 2020), and that PDZD8-deficient ($PDZD8^{-/-}$) mice exhibit brain-specific accumulation of CEs due to impaired lipophagy—a form of microautophagy in which lipid droplets directly fuse with lysosomes for degradation by lysosomal lipase(Morita et al., 2022). Behavioral battery analysis revealed that $PDZD8^{-/-}$ mice display pronounced

hyperactivity, reduced anxiety and fear, and deficits in fear-conditioned memory and working memory(Kurihara et al., 2023), collectively resembling ADHD-like phenotypes. Moreover, a PDZD8 mutation near the SMP domain has been linked to human intellectual disability, accompanied by regional brain hypertrophy and atrophy(Al-Amri et al., 2022).

Present study

Despite these findings, the specific brain regions and neural circuits affected by PDZD8 deficiency remained unclear. Here, we demonstrate that PDZD8$^{-/-}$ mice exhibit marked lipid accumulation in the SNr, a major output nucleus of the basal ganglia. This lipid deposition disrupts the striato–nigro–thalamo–cortical circuitry, leading to disinhibition of dopaminergic neurons and maladaptive reinforcement of striatal inhibitory feedback. These results provide the first evidence that abnormal lipid metabolism in the SNr can remodel basal ganglia circuits, offering new insights into the mechanistic links between lipid dysregulation, dopaminergic imbalance, and ADHD-like behavioral phenotypes.

RESULTS

PDZD8 expression in midbrain neurons and astrocytes

We performed immunostaining using the PDZD8 antibody in PDZD8$^{+/+}$ and PDZD8$^{-/-}$ mice to comprehensively analyze the distribution of PDZD8 expression in the brain. Though the specificity of the PDZD8 antibody has been demonstrated in a previous paper (Morita et al., 2022), we compared PDZD8$^{+/+}$ and PDZD8$^{-/-}$ signals in each region and only considered cells with specific signals as PDZD8-expressing cells (Supplementary figure 1A). The results showed that PDZD8 is expressed in multiple regions throughout the brain, but the intensity of expression varied considerably depending on the region and cell type. Brain regions showing notably high expression are shown in Supplementary figure 1B.

To determine the cellular distribution of PDZD8, we examined its expression in the midbrain of wild-type mice. PDZD8 was abundantly expressed in SNc, VTA, and SNr, regions defined by dopamine transporter (DAT) expression (Figure 1A). In the SNc and VTA, PDZD8 was localized in DAT- and tyrosine hydroxylase (TH)-positive dopaminergic neurons, respectively (Figure 1B, C). In contrast, PDZD8 was expressed in PV-positive GABAergic neurons and glial fibrillary acidic protein (GFAP)-positive astrocytes within the SNr (Figure 1D, E). Though the SNr is a large region with distinct cellular distributions according to rostral, caudal, medial, and lateral areas, we selected regions for high concordance between PDZD8 and each cell marker. These findings indicate that PDZD8 is highly distributed across neuronal and glial populations around the substantia nigra in midbrain, suggesting its potential role in modulating dopaminergic

circuitry.

Marked lipid accumulation in SNr in PDZD8$^{-/-}$ mice

Given that PDZD8$^{-/-}$ mice exhibit abnormal CE accumulation in the brain, we next identified the affected brain regions. LipiDye II staining revealed significant lipid accumulation in several areas, including SNr, dorsal raphe (DR), basolateral amygdala (BLA), and central amygdala (CeA), with the SNr showing the most prominent signal (Figure 2A). These results were confirmed by LipiDye II and LipidTOX staining, both of them specifically labels neutral lipids in the hydrophobic core of LDs with a high signal-to-noise ratio (Figure 2B, C). High-resolution Z-stack imaging demonstrated dense intracellular lipid droplets, likely representing lipofuscin, within SNr cells (Figure 2D). Thus, the SNr represents the principal site of lipid deposition in PDZD8$^{-/-}$ mice.

Lipofuscin deposits are enriched in SNr in PDZD8$^{-/-}$ mice

To characterize the lipid deposits in greater detail, serial midbrain sections were stained with LipiDye II and anti-DAT. Large lipid deposits were concentrated in the caudal SNr, while smaller aggregates appeared rostrally (Figure 3A). Ectopic anti-DAT signals were detected in PDZD8$^{-/-}$ SNr, especially in caudal regions, likely overlapping with LipiDye II fluorescence (Figure 3B). Then triple labeling with LipiDye II, DAT, and GFAP confirmed complete overlap of these signals, consistent with autofluorescent lipofuscin (Figure 3C). These results demonstrate that most large lipid deposits in the caudal SNr of PDZD8$^{-/-}$ brain are lipofuscin.

Extracellular and intracellular lipid deposits in SNr in PDZD8$^{-/-}$ mice

Z-stack 3D imaging combined with GFAP staining revealed two types of lipid deposits in the SNr of PDZD8-/- mice: small extracellular deposits, likely lipoproteins, and large intracellular deposits, likely lipofuscin (Figure 4A–C). Extracellular deposits were more abundant medially, while intracellular deposits predominated laterally. 3D reconstructions further distinguished intra- versus extracellular localization (Supplementary movies A, B). Notably, intracellular lipofuscin overlapped with GFAP signals, suggesting autofluorescent properties of astrocytic lipofuscin.

Increased striatal projection to SNr in PDZD8$^{-/-}$ mice

To test whether lipid accumulation alters SNr connectivity, we performed retrograde neuronal tracing by injecting Alexa594-CTb into the SNr of PDZD8$^{+/+}$ and PDZD8$^{-/-}$ mice (Figure 5A, B). In both genotypes, injection sites were equivalent. However, corpus striatal (CP) neurons, including pallidum (GP) neurons, projecting to SNr were markedly increased and spatially expanded in PDZD8$^{-/-}$ mice (Figure 5C–E). In addition, we also observed the similar results with a different mouse pair using the alternative tracer Alexa488-CTb (Supplementary figure 2A–E). These changes indicate enhanced striatal

186 inputs to the SNr (Figure 5F). PDZD8 expression was also detected in dopamine- and
187 cAMP-regulated phosphoprotein (DARPP-32)-positive medium spiny neurons (MSNs)
188 in the striatum (Figure 5G), and DARPP-32 immunoreactivity was significantly elevated
189 in the SNr of PDZD8$^{-/-}$ mice (Figure 5H). Together, these findings suggest strengthened
190 GABAergic striatal inputs to SNr in PDZD8 deficiency.

191 **Decreased projection from SNr in PDZD8$^{-/-}$ mice.**

192 Given that SNr serves as a major output nucleus of the basal ganglia that regulates both
193 thalamic and midbrain dopaminergic neurons, we examined downstream projections by
194 injection of anterograde neuronal tracer palmitoylated GFP (palGFP) into the SNr of
195 PDZD8$^{+/+}$ and PDZD8$^{-/-}$ mice. Injection sites were comparable between groups (Figure
196 6A, B). In PDZD8$^{-/-}$ mice, projections from the SNr to the VAL/VM and nst (Figure 6C),
197 as well as to the VTA and SNc (Figure 6D), were markedly reduced compared to controls
198 (Figure 6E), indicating disrupted SNr output (Figure 6F). Although GPi is also a major
199 output nucleus from SNr, palGFP signal in GPi was too faint to determine whether there
200 was a difference between PDZD8$^{+/+}$ and PDZD8$^{-/-}$.

201 **Abnormal dopaminergic circuits in PDZD8$^{-/-}$ mice**

202 Based on these observations, we propose that lipid accumulation in the SNr induces
203 functional disinhibition within the basal ganglia–thalamocortical circuitry (Figure 7).
204 Specifically, lipid deposition in SNr neurons leads to reduced inhibitory output from the
205 SNr to both VAL/VM and the nst, as well as to the VTA and SNc. The
206 consequent disinhibition of thalamic and dopaminergic targets results in hyperactivation
207 of dopaminergic neurons, which in turn enhances inhibitory feedback from striatal
208 GABAergic neurons to SNr, thereby reinforcing the suppression of SNr output. This
209 establishes a maladaptive feedback loop—reduced SNr–thalamic output, dopaminergic
210 disinhibition, and strengthened striatal inhibition—that possibly destabilizes the
211 functional balance of the basal ganglia–thalamocortical circuitry. Such large-scale circuit
212 dysregulation likely underlies the abnormal behavioral phenotypes observed in PDZD8$^{-/-}$
213 mice, including hyperactivity, reduced anxiety and fear, and impaired fear-memory
214 regulation.

215

216 **DISCUSSION**

217 **Summary of the findings**

218 In this study, we identified a crucial role of the lipid transport protein PDZD8 in
219 maintaining basal ganglia circuit homeostasis. PDZD8 deficiency led to prominent lipid
220 accumulation in the SNr, accompanied by structural and functional remodeling of basal
221 ganglia output pathways. Neuronal tracing analyses revealed reduced SNr projections to

222 both thalamic (VAL/VM, nst) and midbrain dopaminergic targets (VTA, SNc), together
223 with enhanced inhibitory input from striatal GABAergic neurons. These anatomical
224 changes were consistent with functional disinhibition of dopaminergic circuits, resulting
225 in hyperactivation of dopaminergic neurons and maladaptive reinforcement of striatal
226 inhibition. Given that PDZD8$^{-/-}$ mice exhibit hyperactivity and reduced anxiety and fear
227 at the behavioral level—features reminiscent of ADHD-like phenotypes—these findings
228 establish a direct mechanistic link between lipid metabolic disruption in the SNr, basal
229 ganglia circuit disinhibition, and behavioral dysregulation.

230 **SNr lipid accumulation and circuit disinhibition**

231 The SNr serves as a tonic inhibitory gate in the cortico–basal ganglia–thalamo–cortical
232 loop (basal ganglia–thalamocortical circuit), controlling both motor and cognitive outputs.
233 Our data suggest that lipid accumulation within SNr neurons compromises this inhibitory
234 control, likely by affecting cellular excitability and synaptic output. Lipofuscin-like
235 deposits, enriched in cholesteryl esters and peroxidized lipids, are known to induce
236 lysosomal stress, oxidative imbalance, and altered membrane conductance. These effects
237 may collectively reduce the firing capacity or GABA release efficacy of SNr neurons,
238 thereby reducing inhibitory output to their downstream targets. The observed reduction
239 of SNr projections to VAL/VM and nst implies a loss of inhibitory tone at the thalamic
240 level, which would increase cortical excitability and contribute to hyperactivity. Similarly,
241 decreased inhibition of VTA and SNc dopaminergic neurons produces dopaminergic
242 disinhibition, leading to excessive dopamine release in the striatum. The resulting
243 dopaminergic hyperactivation enhances corticostriatal drive, which strengthens striatal
244 GABAergic feedback to the SNr. This closed-loop maladaptive feedback—SNr
245 hypoactivity, dopaminergic hyperactivation, and enhanced striatal inhibition—creates a
246 self-reinforcing circuit instability. Such loop-level dysregulation likely underlies the
247 behavioral abnormalities observed in PDZD8$^{-/-}$ mice.

248 **Disinhibition-driven distortion of RPE signaling in the VTA–BLA circuit**

249 Beyond basal ganglia output pathways, the disinhibition of dopaminergic neurons
250 observed in PDZD8$^{-/-}$ mice likely extends its impact to broader reward-related networks,
251 particularly the VTA–BLA circuit, which encodes reward prediction error (RPE) signals
252 during associative learning. The VTA conveys phasic dopamine release to the BLA during
253 both appetitive and aversive conditioning, where dopaminergic modulation shapes the
254 associative strength between conditioned and unconditioned stimuli. Disruption of
255 inhibitory control from the SNr to midbrain dopaminergic neurons may bias RPE
256 computation—amplifying positive prediction signals while diminishing aversive or
257 omission-related responses. Such imbalance could account for the hyperactivity and

258 impaired fear memory observed in PDZD8$^{-/-}$ mice, reflecting aberrant valuation of
259 outcomes and a failure to encode negative prediction errors. In this framework, lipid
260 accumulation–induced disinhibition of the SNr may distort dopaminergic gain control
261 within the VTA–BLA network, leading to maladaptive reinforcement learning and
262 emotional dysregulation. This suggests that PDZD8-dependent lipid homeostasis in the
263 SNr is essential for maintaining the dynamic balance between positive and negative RPE
264 signaling across cortico–amygdalo–dopaminergic loops.

265 **Comparison with prior studies on basal ganglia and ADHD**

266 Our findings extend previous evidence implicating SNr dysfunction in the
267 pathophysiology of ADHD. Earlier studies demonstrated that H_2R deficiency in PV^+
268 neurons of the SNr reduces inhibitory output and induces hyperactivity and impulsivity.
269 Similarly, reduced GABAergic tone and enhanced dopaminergic transmission have been
270 reported in ADHD patients and model animals. The present work suggests that lipid
271 metabolic stress may represent a previously unrecognized upstream mechanism
272 producing a similar disinhibitory outcome. PDZD8 is an ER–endosome tethering protein
273 required for lipid transport and membrane contact site integrity. Loss of PDZD8 impairs
274 lipophagy, leading to intracellular lipid droplet accumulation and lipofuscin formation.
275 These pathological deposits are not inert: they alter calcium handling, disrupt
276 mitochondrial dynamics, and perturb synaptic vesicle turnover. The convergence of
277 lysosomal and GABAergic dysfunction in SNr neurons likely explains the observed
278 circuit-level changes. Therefore, disinhibition of SNr neurons emerges as a new paradigm
279 linking lipid homeostasis to dopaminergic regulation and behavioral control. However,
280 areas beyond those shown in this study may also be involved in ADHD-like behavior of
281 PDZD8$^{-/-}$. While lipid accumulation in PDZD8$^{-/-}$ is most pronounced in SNr, significant
282 lipid accumulation is also observed in DR, BLA, and CeA (Figure 2A). Therefore, future
283 studies should investigate abnormalities in regions beyond SNr. ADHD is primarily
284 considered a dysfunction of circuits connecting PFC and basal ganglia, which govern
285 attention and executive function, with dopamine and noradrenaline involved in
286 controlling these circuits. Furthermore, amygdala, which regulates emotions, and raphe
287 nuclei, which control impulsivity, are also implicated in ADHD, with serotonin involved
288 in regulation of these circuits. It is necessary to investigate abnormalities in these circuits
289 and neurotransmitters in PDZD8$^{-/-}$ mice.

290 **Regulation of inhibitory circuits by lipid metabolism**

291 Although direct evidence for lipid deposition within neurons in PDZD8$^{-/-}$ has not been
292 obtained, the morphology and size of lipid-accumulating cells in PDZD8$^{-/-}$ mice suggest
293 they must be neurons. For example, in Figure 4C (LipiDyeII+GFAP), the two central

white cells exhibit the characteristic pyramidal shape of neurons, with a cell body diameter exceeding 10 μm, significantly larger than the size of astrocyte cell bodies, which have a diameter of 5 μm or less. Similarly, in Figure 2D (LipiDyeII+DIC), lipid-accumulating cells in PDZD8$^{-/-}$ also exhibit the morphology and size of pyramidal cells thought to be neurons. Lipid homeostasis is increasingly recognized as a determinant of neuronal function. Our findings highlight that inhibitory GABAergic circuits are particularly sensitive to metabolic stress. The SNr, characterized by high tonic firing rates, may be especially vulnerable to disruptions in lipid trafficking and degradation. Accumulation of peroxidized lipids and lipofuscin can impair GABA release machinery and ion channel stability, thereby compromising tonic inhibition. Astrocytic PDZD8 expression observed in our study suggests that glia–neuron lipid coupling may be essential for maintaining SNr function. Disruption of such glial lipid buffering could amplify local oxidative stress and propagate dysfunction across the basal ganglia network.

Implications for neuropsychiatric and neurodegenerative disorders

The link between lipid accumulation and circuit disinhibition identified here may have broader implications beyond ADHD. Lipofuscin accumulation and lysosomal dysfunction are hallmarks of Alzheimer's disease and aging-related cognitive decline. The present findings suggest that even in the absence of overt neurodegeneration, lipid metabolic perturbations can remodel inhibitory circuits and alter behavioral state. Given the prominent dopaminergic involvement, PDZD8 dysfunction may represent a shared vulnerability factor bridging metabolic stress, dopamine dysregulation, and cognitive-behavioral disorders related to basal ganglia or SNr.

Limitation of the study

Lipofuscin emits autofluorescence, so it has not been proven that lipid-accumulating cells in PDZD8$^{-/-}$ mice are neurons. A method for observing lipofuscin using a specific wavelength filter in immunostaining has also been reported (Guo, Cell, 2025), but we have not succeeded in this approach and need to establish the method in the future.

Though the quantitative analysis for entire SNr region (Figure 2A) had been demonstrated, those for the series of slices (Figure 3) or for the 3D images (Figure 4) of SNr are also important.

Although the causal relationship and mechanism for circuit reorganization due to lipid accumulation in PDZD8$^{-/-}$ remain unproven, previous studies have reported that "excessive lipofuscin accumulation generates reactive oxygen species via lipid peroxidation, inducing lysosomal stress and chronic neuroinflammation, thereby promoting neurodegeneration (Terman, 2004; Gray, 2005; Moreno-García, 2018; Guo, Cell, 2025)." Thus, we propose a hypothesis consistent with this. In the future,

quantification of intracellular lipid peroxides and reactive oxygen species will be necessary.

Experiments measuring levels of dopamine or dopamine metabolites are important but technically challenging and cannot be performed at this time. This needs to be clarified in the future.

Although PDZD8 is broadly expressed across multiple brain regions, prominent lipid accumulation occurred selectively in the SNr of PDZD8$^{-/-}$ mice. The regional vulnerability underlying this selectivity remains unresolved and warrants further investigation, including the potential involvement of PDZD8-interacting complex components. Future studies combining in vivo imaging of dopamine dynamics, electrophysiological recordings of SNr neurons, and cell-type–specific PDZD8 rescue in neuronal versus glial populations will be essential to delineate the relative contributions of each cell type. Moreover, pharmacological or genetic interventions aimed at restoring lipid homeostasis may help determine whether normalization of lipid metabolism can rescue basal ganglia circuit stability and behavioral deficits.

Conclusion

Together, our findings reveal that PDZD8-dependent lipid metabolism is indispensable for preserving inhibitory control within the basal ganglia and ensuring accurate dopaminergic prediction error signaling, providing a unifying mechanistic framework linking metabolic stress, circuit disinhibition, and behavioral dysregulation.

METHODS

Animals

Mice were housed under 12-h light/dark cycle with food and water ad libitum. All mouse experiments were approved by the animal ethics committee of Nagoya City University. All experiments were performed using at least two sets of paired mice (PDZD8$^{+/+}$ and PDZD8$^{-/-}$). Mouse sex and age were matched across experiments, and both mice in each pair were analyzed simultaneously. In all experiments, mice were aged 4–9 months and were either male or female. Figures show representative images from one of the multiple experiments performed. A summary table listing these mouse details was added to Supplementary table 1.

Mutant mice

Generation of PDZD8-KO mice was described previously(Morita et al., 2022). In brief, Cas9 nickase mRNA, Generic tracrRNA, and target-specific crRNA were mixed and injected into C57BL/6J mouse zygotes. The resultant mutant mice were backcrossed with C57BL/6J mice before experiments. Animals were genotyped by PCR analysis.

366 **Antibodies and reagents**
367 Rabbit polyclonal antibodies to PDZD8 were from Sigma-Aldrich; mouse monoclonal
368 antibodies to TH were from Sigma-Aldrich; mouse monoclonal antibodies to GFAP
369 were from Proteintech; guinea pig polyclonal antibodies to DAT, PV, and DARPP were
370 from Frontier institute; Alexa Fluor 488 goat anti-rabbit IgG, Alexa Fluor 555 goat anti-
371 mouse IgG, Alexa Fluor 555 goat anti-guinea pig IgG, LipidTox, and Alexa Fluor 594
372 cholera toxin B were from Thermo Fisher Scientific; LipiDye II was from Funakoshi.
373 **Immunohistofluorescence analysis**
374 Mouse brain was fixed with 2% paraformaldehyde in phosphate-buffered saline (PBS,
375 Wako), exposed consecutively to 15% and 30% sucrose in PBS for 2 days, and
376 embedded in tissue-Tek OCT compound (SAKURA). Thin sections were prepared with
377 a cryostat microtome (CM1850 UV, Leica) and stained consecutively with primary
378 antibodies and Alexa Fluor–labeled secondary antibodies in PBS containing 0.5% Triton
379 X-100, or stained with LipiDye II or LipidTox in PBS. The sections were observed with
380 an LSM800 confocal microscope (Zeiss), and the images were processed for calculation
381 of fluorescence intensity with ZEN imaging software (Zeiss). Brain regions were
382 referenced from Allen Brain Atlas (http://atlas.brain-map.org).
383 **Stereotaxic injection**
384 Mice were anesthetized intraperitoneally with a mixture of midazolam (4 mg kg^{-1},
385 SANDOZ, Tokyo, Japan), medetomidine (0.75 mg kg^{-1}, Kyoritsu Seiyaku, Tokyo,
386 Japan) and butorphanol (5 mg kg^{-1}, Meiji Seika Pharma, Tokyo, Japan) and placed in a
387 stereotaxic frame (NARISHIGE, Tokyo, Japan). Body temperature was maintained at
388 37 °C. The scalp was sterilized and incised, and a small craniotomy was made above the
389 target. Alexa Fluor 594– or 488–conjugated cholera toxin subunit B (CTb, Thermo
390 Fisher Scientific, MA, USA) was prepared at 2 μg μL^{-1} in sterile PBS. AAV2-CMV-
391 palGFP virus particles were from Dr. Nakamura(Yahiro et al., 2023). 200 nl of Alexa
392 Fluor 594-CTb was injected into the SNr (coordinates from Bregma: AP: -3.2 mm, ML:
393 ±1.4 mm, DV: -4.4 mm). 150 nl of Alexa Fluor 488-CTb was injected into the SNr
394 (coordinates from Bregma: AP: -3.7 mm, ML: ±1.8 mm, DV: -4.5 mm). 100 nl of AAV
395 solution was injected into the SNr (coordinates from Bregma: AP: -3.7 mm, ML: ±1.8
396 mm, DV: -4.5 mm). Tracer (200 nL per site) was delivered using a Hamilton
397 microsyringe (1701RN Neuros Syringe, 33G; Hamilton Company, NV, USA) connected
398 to a motorized stereotaxic microinjector (NARISHIGE, Tokyo, Japan ; 100 nL min^{-1}).
399 After infusion, the needle was left in place for 10–15 min to minimize reflux before
400 being withdrawn slowly. For each mouse, injections were made at the following
401 stereotaxic coordinates relative to bregma: [AP -3.2], [ML ±1.4], [DV -4.4] (mm). The

scalp was closed with sutures, and mice were monitored until full recovery. After surgery, mice received postoperative care including an intraperitoneal injection of antibiotic (amoxicillin, Kyoritsu Seiyaku, Tokyo, Japan; 50 mg kg^{-1}, i.p.). Information of tracer injection was summarized in Supplementary table 2.

Histological analysis of neural tracing

Mouse brain was fixed with 2% paraformaldehyde in PBS, exposed consecutively to 15% and 30% sucrose in PBS for 2 days, and embedded in OCT compound. Thin sections (50 μm) were prepared with a cryostat microtome. The sections were observed with an LSM800 confocal microscope. The distribution of the tracer at the injection site was verified, and only sections without substantial displacement of the injection site were included in the analysis. The sections were imaged using a LSM800 to acquire fluorescence images. The images were processed for calculation of fluorescence intensity with ZEN imaging software. Regions of interest (ROIs) were defined on the acquired images, and fluorescence intensity values were extracted. Background fluorescence was subtracted to obtain tracer-specific signal intensities. Tracer signals were quantified for both the injection sites and the target regions, and values from the target regions were normalized to those of the corresponding injection sites.

Statistical analysis

For lipid imaging, statistical analysis was performed with the use of BellCurve for Excel software (Social Survey Research Information, Tokyo, Japan). Normality of data was assessed with the Shapiro-Wilk test. If the normality was not met, the Mann-Whitney U test was applied (Fig. 2A, SNr; DR; BLA). If data were normally distributed and variance was homogeneous between genotypes, comparisons were performed with Student's *t* test. If homogeneity of variance was not assumed, Welch's *t* test was applied instead of Student's *t* test (Fig. 2A, CeA). For neuronal tracing, statistical analysis was performed using Microsoft Excel. Variance homogeneity was assessed using an F-test, and based on the results, appropriate t-tests, Welch's t test (Fig. 6E, VAL/VM; SNc) or Student's t test (Fig. 5E, Str; Fig. 6E, VTA; SNc) were applied to evaluate statistical significance. Quantitative data are presented as mean ± SE. Statistical significance of a *P* value is indicated as $p < 0.05$ (*) and $p < 0.001$ (***). Sample size (*n*) are in the figure legends.

Acknowledgements

We thank K. Nakamura for AAV2-CMV-palGFP virus particles, I. Yamahata for Immunohistofluorescence analysis, and the Research Equipment Sharing Center at Nagoya City University for assistance.

Author contributions statement

M.S. conceptualized and supervised the study, acquired funding, designed experiments, and wrote the manuscript; T.O., Y.M., M.K., and H.T. performed experiments; M.I. and H.M. prepared resources.

Funding information

This work was supported in part by KAKENHI grants from Japan Society for the Promotion of Science (JSPS) to M.S. (24K02122).

Ethics

The animal study was approved by Nagoya City University, Animal Research Committee. The study was conducted in accordance with the local legislation and institutional requirements.

Data availability and sources

The original contributions presented in the study are included in the article/ supplementary material, further inquiries can be directed to the corresponding author.

REFERENCES

Al-Amri, A.H., Armstrong, P., Amici, M., Ligneul, C., Rouse, J., El-Asrag, M.E., et al. (2022). PDZD8 Disruption Causes Cognitive Impairment in Humans, Mice, and Fruit Flies. *Biol Psychiatry* 92(4)**,** 323-334. doi: 10.1016/j.biopsych.2021.12.017.

Alexander, G.E., DeLong, M.R., and Strick, P.L. (1986). Parallel organization of functionally segregated circuits linking basal ganglia and cortex. *Annu Rev Neurosci* 9**,** 357-381. doi: 10.1146/annurev.ne.09.030186.002041.

An, D., You, Y., Ma, Q., Xu, Z., Liu, Z., Liao, R., et al. (2025). Deficiency of histamine H(2) receptors in parvalbumin-positive neurons leads to hyperactivity, impulsivity, and impaired attention. *Neuron* 113(4)**,** 572-589 e576. doi: 10.1016/j.neuron.2024.12.002.

Biederman, J. (2005). Attention-deficit/hyperactivity disorder: a selective overview. *Biol Psychiatry* 57(11)**,** 1215-1220. doi: 10.1016/j.biopsych.2004.10.020.

Blanchard, J.W., Akay, L.A., Davila-Velderrain, J., von Maydell, D., Mathys, H., Davidson, S.M., et al. (2022). APOE4 impairs myelination via cholesterol dysregulation in oligodendrocytes. *Nature* 611(7937)**,** 769-779. doi: 10.1038/s41586-022-05439-w.

474 Dahm, R. (2006). Alzheimer's discovery. *Curr Biol* 16(21), R906-910. doi:
475 10.1016/j.cub.2006.09.056.
476 Falasconi, A., Kanodia, H., and Arber, S. (2025). Dynamic basal ganglia output signals
477 license and suppress forelimb movements. *Nature* 644(8077), 749-758. doi:
478 10.1038/s41586-025-09066-z.
479 Foley, P. (2010). Lipids in Alzheimer's disease: A century-old story. *Biochim Biophys Acta*
480 1801(8), 750-753. doi: 10.1016/j.bbalip.2010.05.004.
481 Foster, N.N., Barry, J., Korobkova, L., Garcia, L., Gao, L., Becerra, M., et al. (2021). The
482 mouse cortico-basal ganglia-thalamic network. *Nature* 598(7879), 188-194. doi:
483 10.1038/s41586-021-03993-3.
484 Gray, D.A., and Woulfe, J. (2005). Lipofuscin and aging: a matter of toxic waste. *Sci*
485 *Aging Knowledge Environ* 2005(5), re1. doi: 10.1126/sageke.2005.5.re1.
486 Grillner, S., and Robertson, B. (2016). The Basal Ganglia Over 500 Million Years. *Curr*
487 *Biol* 26(20), R1088-R1100. doi: 10.1016/j.cub.2016.06.041.
488 Guo, J.L., Braun, D., Fitzgerald, G.A., Hsieh, Y.T., Rouge, L., Litvinchuk, A., et al. (2025).
489 Decreased lipidated ApoE-receptor interactions confer protection against
490 pathogenicity of ApoE and its lipid cargoes in lysosomes. *Cell* 188(1), 187-206
491 e126. doi: 10.1016/j.cell.2024.10.027.
492 Kim, H., Ahrlund-Richter, S., Wang, X., Deisseroth, K., and Carlen, M. (2016). Prefrontal
493 Parvalbumin Neurons in Control of Attention. *Cell* 164(1-2), 208-218. doi:
494 10.1016/j.cell.2015.11.038.
495 Kurihara, Y., Mitsunari, K., Mukae, N., Shoji, H., Miyakawa, T., and Shirane, M. (2023).
496 PDZD8-deficient mice manifest behavioral abnormalities related to emotion,
497 cognition, and adaptation due to dyslipidemia in the brain. *Mol Brain* 16(1), 11.
498 doi: 10.1186/s13041-023-01002-4.
499 Lambert, J.C., Ibrahim-Verbaas, C.A., Harold, D., Naj, A.C., Sims, R., Bellenguez, C., et
500 al. (2013). Meta-analysis of 74,046 individuals identifies 11 new susceptibility
501 loci for Alzheimer's disease. *Nat Genet* 45(12), 1452-1458. doi: 10.1038/ng.2802.
502 Lee, J., Wang, W., and Sabatini, B.L. (2020). Anatomically segregated basal ganglia
503 pathways allow parallel behavioral modulation. *Nat Neurosci* 23(11), 1388-1398.
504 doi: 10.1038/s41593-020-00712-5.
505 Lewis, D.A., Hashimoto, T., and Volk, D.W. (2005). Cortical inhibitory neurons and
506 schizophrenia. *Nat Rev Neurosci* 6(4), 312-324. doi: 10.1038/nrn1648.
507 Litvinchuk, A., Suh, J.H., Guo, J.L., Lin, K., Davis, S.S., Bien-Ly, N., et al. (2024).
508 Amelioration of Tau and ApoE4-linked glial lipid accumulation and
509 neurodegeneration with an LXR agonist. *Neuron* 112(3), 384-403 e388. doi:

10.1016/j.neuron.2023.10.023.
McElvain, L.E., Chen, Y., Moore, J.D., Brigidi, G.S., Bloodgood, B.L., Lim, B.K., et al. (2021). Specific populations of basal ganglia output neurons target distinct brain stem areas while collateralizing throughout the diencephalon. *Neuron* 109(10), 1721-1738 e1724. doi: 10.1016/j.neuron.2021.03.017.
Moreno-Garcia, A., Kun, A., Calero, O., Medina, M., and Calero, M. (2018). An Overview of the Role of Lipofuscin in Age-Related Neurodegeneration. *Front Neurosci* 12, 464. doi: 10.3389/fnins.2018.00464.
Morita, K., Wada, M., Nakatani, K., Matsumoto, Y., Hayashi, N., Yamahata, I., et al. (2022). PDZD8-deficient mice accumulate cholesteryl esters in the brain as a result of impaired lipophagy. *iScience* 25(12), 105612. doi: 10.1016/j.isci.2022.105612.
Nugent, A.A., Lin, K., van Lengerich, B., Lianoglou, S., Przybyla, L., Davis, S.S., et al. (2020). TREM2 Regulates Microglial Cholesterol Metabolism upon Chronic Phagocytic Challenge. *Neuron* 105(5), 837-854 e839. doi: 10.1016/j.neuron.2019.12.007.
Park, J., Coddington, L.T., and Dudman, J.T. (2020). Basal Ganglia Circuits for Action Specification. *Annu Rev Neurosci* 43, 485-507. doi: 10.1146/annurev-neuro-070918-050452.
Rizzi, G., and Tan, K.R. (2019). Synergistic Nigral Output Pathways Shape Movement. *Cell Rep* 27(7), 2184-2198 e2184. doi: 10.1016/j.celrep.2019.04.068.
Shirane, M., and Nakayama, K.I. (2006). Protrudin induces neurite formation by directional membrane trafficking. *Science* 314(5800), 818-821. doi: 10.1126/science.1134027.
Shirane, M., Wada, M., Morita, K., Hayashi, N., Kunimatsu, R., Matsumoto, Y., et al. (2020). Protrudin and PDZD8 contribute to neuronal integrity by promoting lipid extraction required for endosome maturation. *Nat Commun* 11(1), 4576. doi: 10.1038/s41467-020-18413-9.
Sohal, V.S., Zhang, F., Yizhar, O., and Deisseroth, K. (2009). Parvalbumin neurons and gamma rhythms enhance cortical circuit performance. *Nature* 459(7247), 698-702. doi: 10.1038/nature07991.
Terman, A., and Brunk, U.T. (2004). Lipofuscin. *Int J Biochem Cell Biol* 36(8), 1400-1404. doi: 10.1016/j.biocel.2003.08.009.
Thapar, A., and Cooper, M. (2016). Attention deficit hyperactivity disorder. *Lancet* 387(10024), 1240-1250. doi: 10.1016/S0140-6736(15)00238-X.
van der Kant, R., Langness, V.F., Herrera, C.M., Williams, D.A., Fong, L.K., Leestemaker,

Y., et al. (2019). Cholesterol Metabolism Is a Druggable Axis that Independently Regulates Tau and Amyloid-beta in iPSC-Derived Alzheimer's Disease Neurons. *Cell Stem Cell* 24(3)**,** 363-375 e369. doi: 10.1016/j.stem.2018.12.013.

Yahiro, T., Kataoka, N., and Nakamura, K. (2023). Two Ascending Thermosensory Pathways from the Lateral Parabrachial Nucleus That Mediate Behavioral and Autonomous Thermoregulation. *J Neurosci* 43(28)**,** 5221-5240. doi: 10.1523/JNEUROSCI.0643-23.2023.

555 **FIGURE LEGENDS**

556 **Figure 1. PDZD8 is highly expressed in neurons and astrocytes in the midbrain.**
557 Immunofluorescence analysis of wild-type mouse brain.
558 (A) Dopamine transporter (DAT, magenta) and PDZD8 (green) in the midbrain. Regions
559 corresponding to substantia nigra pars compacta (SNc), ventral tegmental area (VTA),
560 and substantia nigra pars reticulata (SNr) are indicated in the DAT image. The merged
561 image is also shown. Scale bars, 200 μm.
562 (B) PDZD8 (green) and DAT (magenta) in SNc.
563 (C) PDZD8 (green) and tyrosine hydroxylase (TH, magenta) in VTA.
564 (D) PDZD8 (green) and parvalbumin (PV, magenta) in SNr.
565 (E) PDZD8 (green) and GFAP (magenta) in SNr. Scale bars, 20 μm (B–E).
566

567 **Figure 2. Lipofuscin deposits are markedly increased in SNr in PDZD8$^{-/-}$ mice.**
568 Lipid aggregate analysis of PDZD8$^{+/+}$ and PDZD8$^{-/-}$ mouse brains.
569 (A) Dot plots showing mean fluorescence intensity of LipiDye II in SNr, dorsal raphe
570 (DR), basolateral amygdala (BLA), and central amygdala (CeA). Schematic brain
571 sections indicate the regions analyzed. Red lines in sagittal sections (upper) indicate the
572 positions of coronal sections (lower), and red boxes mark the analyzed regions. Sample
573 size (*n*) denotes the number of images.
574 (B, C) Confocal images of LipiDye II (B) and LipidTox (C) in SNr. Boxed regions (left)
575 are shown at higher magnification (right). Scale bars, 50 μm (left) and 20 μm (right).
576 (D) High-resolution images of LipiDye II in SNr of PDZD8$^{-/-}$ mice. Boxed regions (left)
577 are shown enlarged (right). A differential interference contrast (DIC) image is also
578 shown. The dotted line outlines a cell periphery densely packed with lipofuscin (right).
579 Scale bars, 5 μm.
580

581 **Figure 3. Lipofuscin deposits are enriched in SNr in PDZD8$^{-/-}$ mice.**
582 Lipid aggregate analysis of SNr in PDZD8$^{+/+}$ and PDZD8$^{-/-}$ mouse brains.
583 (A) Confocal images of DAT (magenta) and LipiDye II (green) in serial sections of SNr
584 from rostral (left) to caudal (right) regions at 240 μm intervals. Scale bars, 100 μm. For
585 PDZD8-/-, enlarged images of LipiDye II are also shown. Scale bars, 20 μm.
586 (B) The merged images of DAT and DIC for the images outlined in (A) in PDZD8$^{+/+}$
587 and PDZD8$^{-/-}$. The merged images of LipiDye II and DIC in PDZD8$^{-/-}$ are also shown.
588 The region of ectopic DAT signal is outlined with a dotted line. Scale bars, 100 μm.
589 (C) Confocal images of LipiDye II (green), DAT (blue), and GFAP (magenta) in SNr in
590 PDZD8$^{-/-}$. The merged image is also shown. Scale bars, 20 μm.

591

592 **Figure 4. Extracellular and intracellular lipid deposits in SNr in PDZD8-/- mice.**
593 (A) Scheme of coronal section containing SNr from mouse brain atlas (left), in which
594 SNr is shown enlarged (right) with the medial (M) and lateral (L) regions indicated.
595 (B, C) 3D images of LipiDye II (green) and GFAP (magenta) in medial (B) and lateral
596 (C) regions of SNr in PDZD8$^{-/-}$ mice, which are reconstructed from z-stack confocal
597 images using Imaris software. Scale bars, 10 μm.
598

599 **Figure 5. Abnormal striatal projection to SNr in PDZD8$^{-/-}$ mice.**
600 (A, B) Confocal images of Alexa594-conjugated cholera toxin subunit B (Alexa594-
601 CTb) injected to SNr merged with DIC images. Tiling images of cerebral hemisphere
602 (A) and serial sections from rostral (left) to caudal (right) regions at 50 μm intervals
603 focusing on SNr (B). Scale bars, 500 μm (A) and 200 μm (B).
604 (C, D) Confocal images of Alexa594-CTb merged with DIC images of brain region
605 containing striatum, indicating projection sources. Tiling images of cerebral hemisphere
606 (C) and serial sections from rostral (left) to caudal (right) regions at 50 μm intervals
607 focusing on striatum (D). Scale bars, 500 μm (C) and 200 μm (D).
608 (E) Dot plots showing normalized ratio of mean fluorescence intensity of Alexa594-
609 CTb at Str (striatum). Sample size (*n*) denotes the number of images.
610 (F) Schematic representation of striatal projections to SNr, with showing increase in
611 PDZD8$^{-/-}$ mice compared to PDZD8$^{+/+}$ mice. Injection sites of Alexa594-CTb to SNr are
612 also indicated.
613 (G) Immunofluorescence images of PDZD8 (green) and dopamine- and cAMP-
614 regulated phosphoprotein (DARPP-32, magenta) in striatum of wild-type mice, with
615 merged image. Scale bars, 20 μm.
616 (H) Immunofluorescence images of DARPP and merged with DIC in SNr of PDZD8$^{+/+}$
617 and PDZD8$^{-/-}$. Scale bars, 100 μm.
618

619 **Figure 6. Abnormal projection from SNr in PDZD8$^{-/-}$ mice.**
620 (A, B) Confocal images showing palmitoylated GFP (palGFP) injection sites in SNr
621 merged with DIC images. Tiling images of cerebral hemisphere (A) and serial sections
622 from rostral (left) to caudal (right) regions at 100 μm intervals focusing on SNr (B).
623 Scale bars, 500 μm (A); 200 μm (B).
624 (C) Confocal and merged DIC images of thalamic regions showing SNr projection
625 targets. PalGFP signals indicate SNr projections to the ventral anterior-lateral complex

626 of the thalamus (VAL), ventromedial thalamus (VM), and the nigrostriatal tract (nst).
627 Scale bars, 200 μm.
628 (D) Confocal and merged DIC images of midbrain regions showing SNr projections to
629 the ventral tegmental area (VTA) and substantia nigra pars compacta (SNc). Scale bars,
630 200 μm.
631 (E) Dot plots showing normalized ratio of mean fluorescence intensity of palGFP at
632 VAL/VM, nst, VTA, and SNc. Sample size (*n*) denotes the number of images.
633 (F) Schematic illustration summarizing the anterograde tracing results. Projections from
634 the SNr to both VM/nst and VTA/SNc are markedly reduced in PDZD8$^{-/-}$ mice
635 compared with PDZD8$^{+/+}$ mice. Injection sites of palGFP in the SNr are indicated.
636
637 **Figure 7. Abnormal dopaminergic circuits in PDZD8$^{-/-}$ mice.**
638 Proposed circuit model depicting the consequences of lipid accumulation in the SNr of
639 PDZD8$^{-/-}$ mice. In PDZD8$^{+/+}$ mice (left), striatal GABAergic inputs transiently inhibit
640 SNr neurons, which tonically suppress activity in thalamic (VM/nst) and midbrain
641 dopaminergic (VTA/SNc) targets, maintaining balanced inhibitory control within the
642 basal ganglia–thalamocortical circuit. In PDZD8$^{-/-}$ mice (right), lipid accumulation in
643 SNr neurons reduces their inhibitory output to VM/nst and VTA/SNc, resulting
644 in functional disinhibition of thalamic and dopaminergic pathways. The consequent
645 hyperactivation of dopaminergic neurons increases dopamine release in the striatum,
646 thereby enhancing inhibitory feedback from striatal neurons to the SNr. This establishes
647 a maladaptive feedback loop—reduced SNr–thalamic output, dopaminergic
648 hyperactivation, and strengthened striatal inhibition—that destabilizes the functional
649 balance of the basal ganglia–thalamocortical circuit and underlies the ADHD-like
650 behavioral abnormalities observed in PDZD8$^{-/-}$ mice.
651
652 **SUPPLEMENTARY FIGURE LEGENDS**
653 **Supplementary figure 1. Specificity of anti-PDZD8 antibody.**
654 (A) Immunofluorescence analysis of PDZD8$^{+/+}$ and PDZD8$^{-/-}$ mice. PDZD8 (green) and
655 the merged image of PDZD8 (green), DAT (red), and Hoechst (blue) in the VTA region
656 are shown. Scale bars, 10 μm.
657 (B) The summary of brain regions and cell types whether they were colocalized or not
658 with PDZD8. Immunostaining with the anti-PDZD8 antibody in PDZD8$^{+/+}$ and
659 PDZD8$^{-/-}$ mice were comprehensively analyzed. (+) in the yellow columns indicates
660 "colocalization was observed between the cell marker and PDZD8". (-) in the white

661 columns indicates "colocalization was not observed between the cell marker and
662 PDZD8". Vacant column indicates "not tested."
663
664 **Supplementary figure 2. Increased striatal projection to SNr in PDZD8$^{-/-}$ mice.**
665 (A, B) Confocal images of Alexa488-CTb injected to SNr merged with DIC images.
666 Tiling images of cerebral hemisphere (A) and images focused on SNr (B). Scale bars,
667 500 μm (A) and 200 μm (B).
668 (C, D) Confocal images of Alexa488-CTb merged with DIC images of brain region
669 containing Str (striatum), indicating projection sources. Tiling images of cerebral
670 hemisphere (C) and images focused on striatum (D). Scale bars, 500 μm (C) and 200
671 μm (D).
672 (E) Dot plots showing normalized ratio of mean fluorescence intensity of Alexa488-
673 CTb at Str (striatum). Sample size (*n*) denotes the number of images.
674
675 **Supplementary figure 3. Decreased SNr projection to thalamus in PDZD8$^{-/-}$ mice.**
676 Confocal and merged DIC images of thalamic regions showing SNr projection targets.
677 PalGFP signals in thalamus indicate SNr projections to the ventral anterior-lateral
678 complex of the thalamus (VAL) and ventromedial thalamus (VM). Scale bars, 200 μm.
679
680 **Supplementary table 1. Information of mouse age and sex.**
681 The age and sex of mice used in this study were summarized.
682
683 **Supplementary table 2. Information of neuronal tracer injection.**
684 Concentration, volume, target region, and coordinates from Bregma for Alexa594-CTb,
685 Alexa488-CTb, and AAV2/1-CMV-palGFP were summarized.
686
687 **Supplementary movie. 3D movies of lipid deposits in SNr in PDZD8$^{-/-}$ mice.**
688 (A, B) 3D movies of LipiDye II (green) and GFAP (magenta) in medial (A) and lateral
689 (B) regions of SNr in PDZD8$^{-/-}$ mice, which are corresponding to Figure 4B and C,
690 respectively. Scale bars, 10 μm.
691

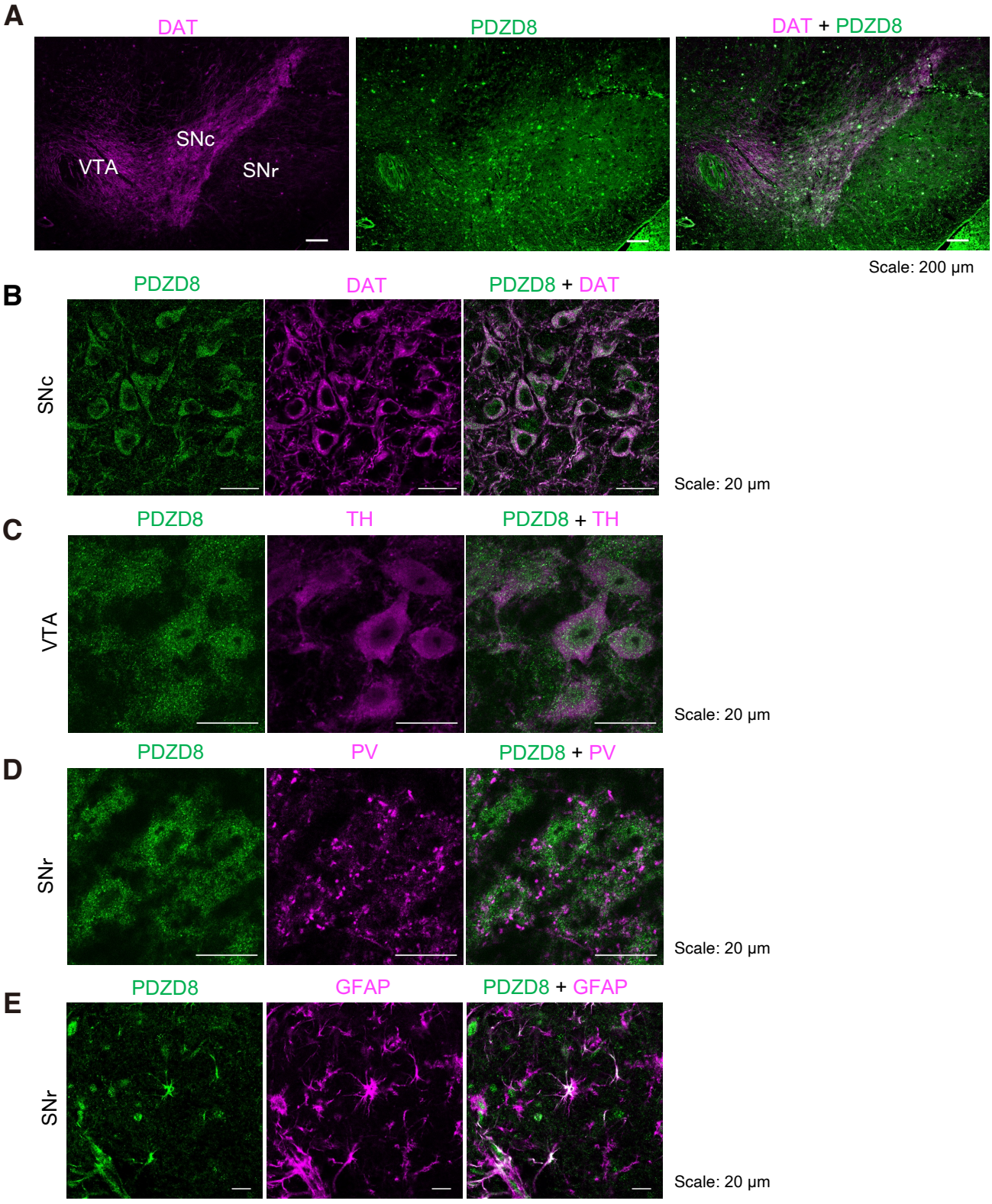
A
DAT
PDZD8
DAT + PDZD8
SNc
VTA
SNr
Scale: 200 μm
B
PDZD8
DAT
PDZD8 + DAT
SNc
Scale: 20 μm
C
PDZD8
TH
PDZD8 + TH
VTA
Scale: 20 μm
D
PDZD8
PV
PDZD8 + PV
SNr
Scale: 20 μm
E
PDZD8
GFAP
PDZD8 + GFAP
SNr
Scale: 20 μm

Figure 1

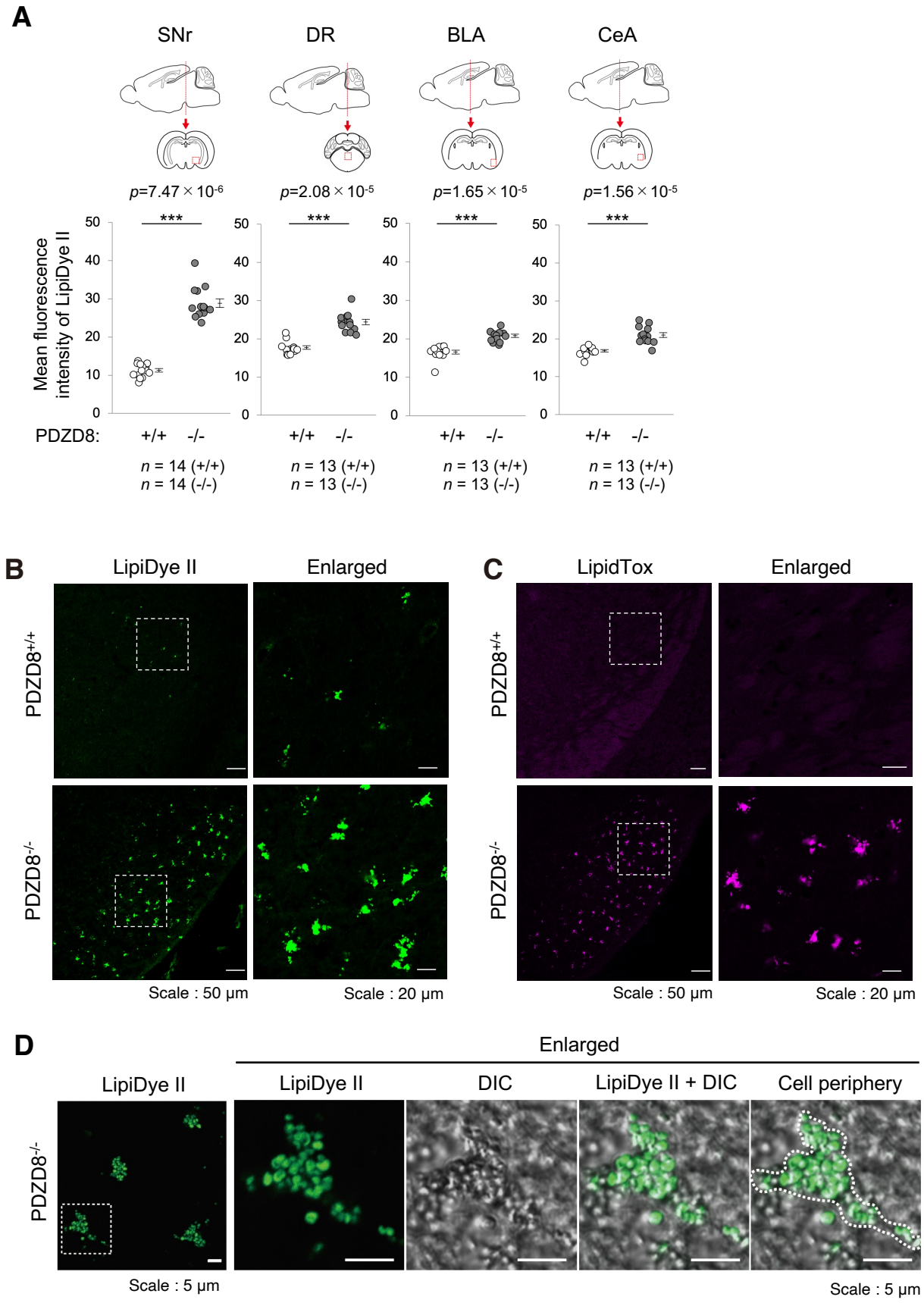
A
SNr
DR
BLA
CeA
p=7.47 × 10-6
p=2.08 × 10-5
p=1.65 × 10-5
p=1.56 × 10-5
***
Mean fluorescence intensity of LipiDye II
PDZD8:
+/+
-/-
n = 14 (+/+)
n = 14 (-/-)
n = 13 (+/+)
n = 13 (-/-)
B
LipiDye II
Enlarged
PDZD8+/+
PDZD8-/-
Scale : 50 μm
Scale : 20 μm
C
LipidTox
Enlarged
PDZD8+/+
PDZD8-/-
Scale : 50 μm
Scale : 20 μm
D
Enlarged
LipiDye II
LipiDye II
DIC
LipiDye II + DIC
Cell periphery
PDZD8-/-
Scale : 5 μm
Scale : 5 μm

Figure 2

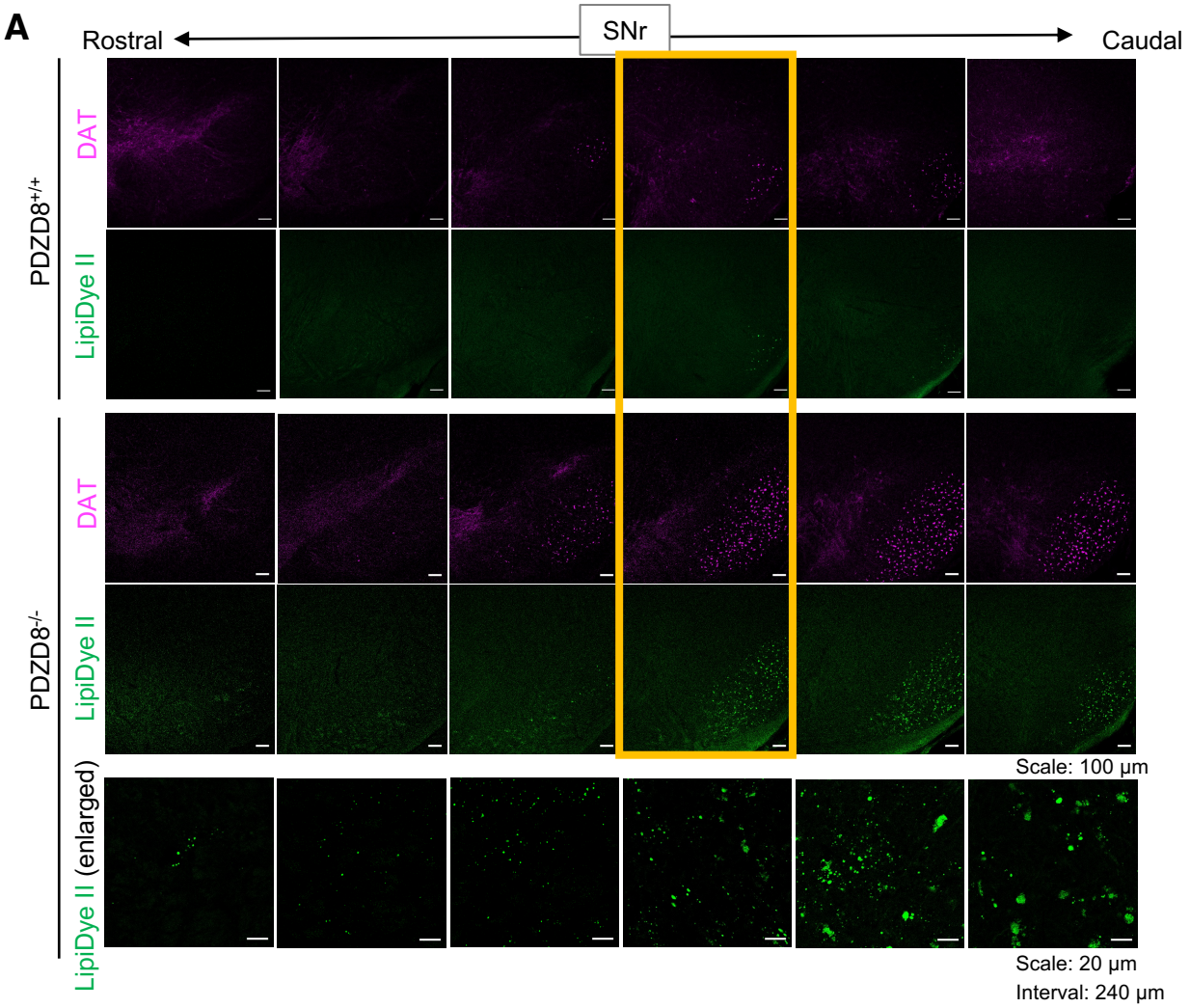
A
Rostral
SNr
Caudal
PDZD8+/+
DAT
LipiDye II
PDZD8-/-
DAT
LipiDye II
LipiDye II (enlarged)
Scale: 100 μm
Scale: 20 μm
Interval: 240 μm

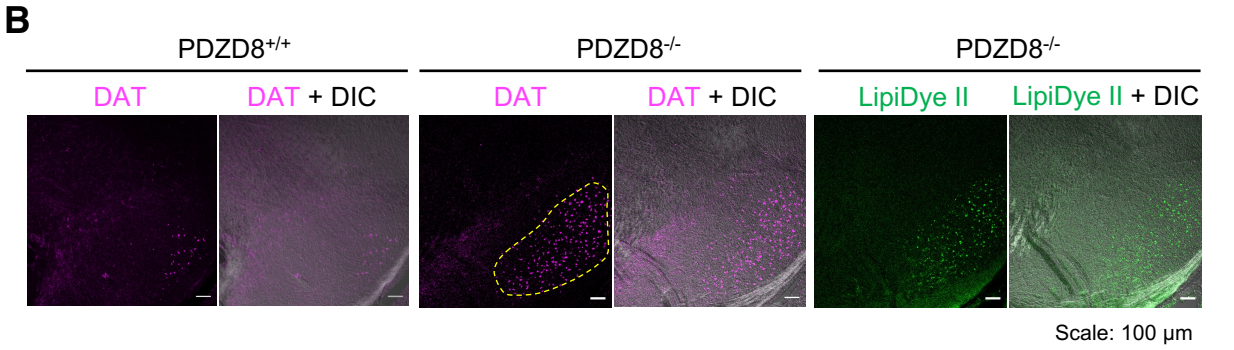
B
PDZD8+/+
PDZD8-/-
PDZD8-/-
DAT
DAT + DIC
DAT
DAT + DIC
LipiDye II
LipiDye II + DIC
Scale: 100 μm

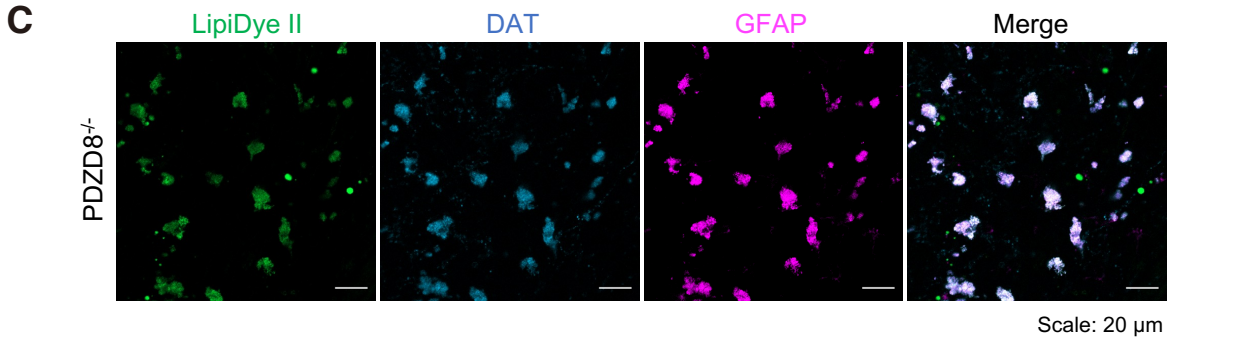
C
LipiDye II
DAT
GFAP
Merge
PDZD8-/-
Scale: 20 μm

Figure 3

A

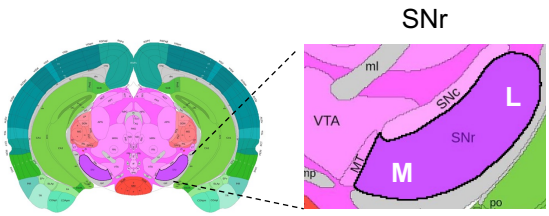

B

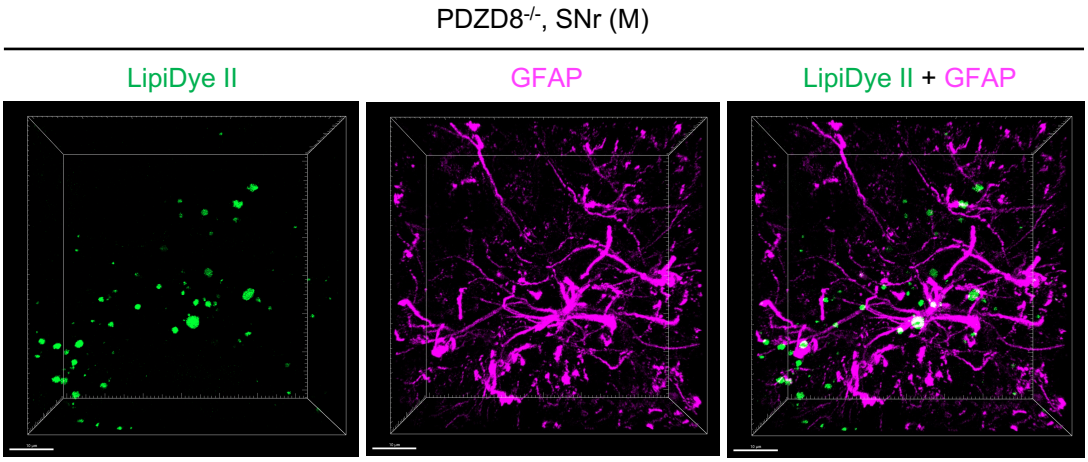

Scale: 10 μm

C

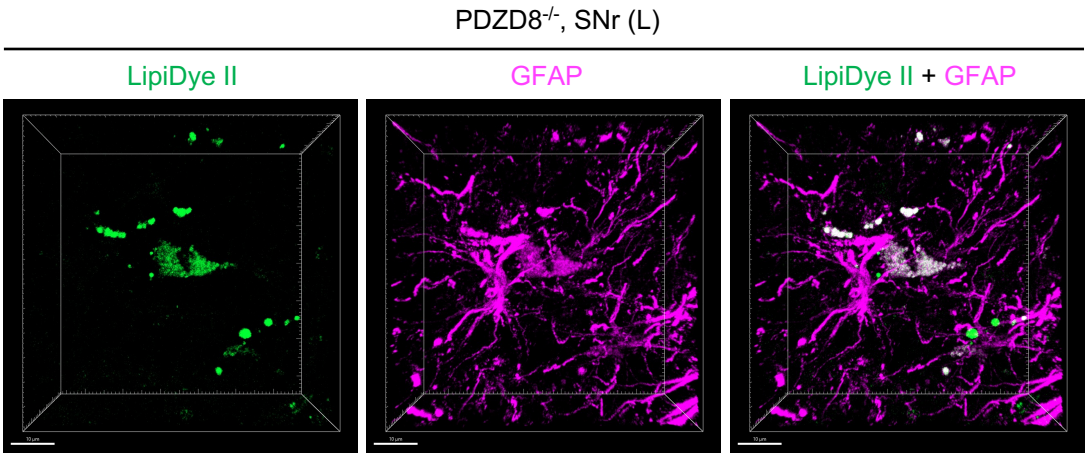

Scale: 10 μm

Figure 4

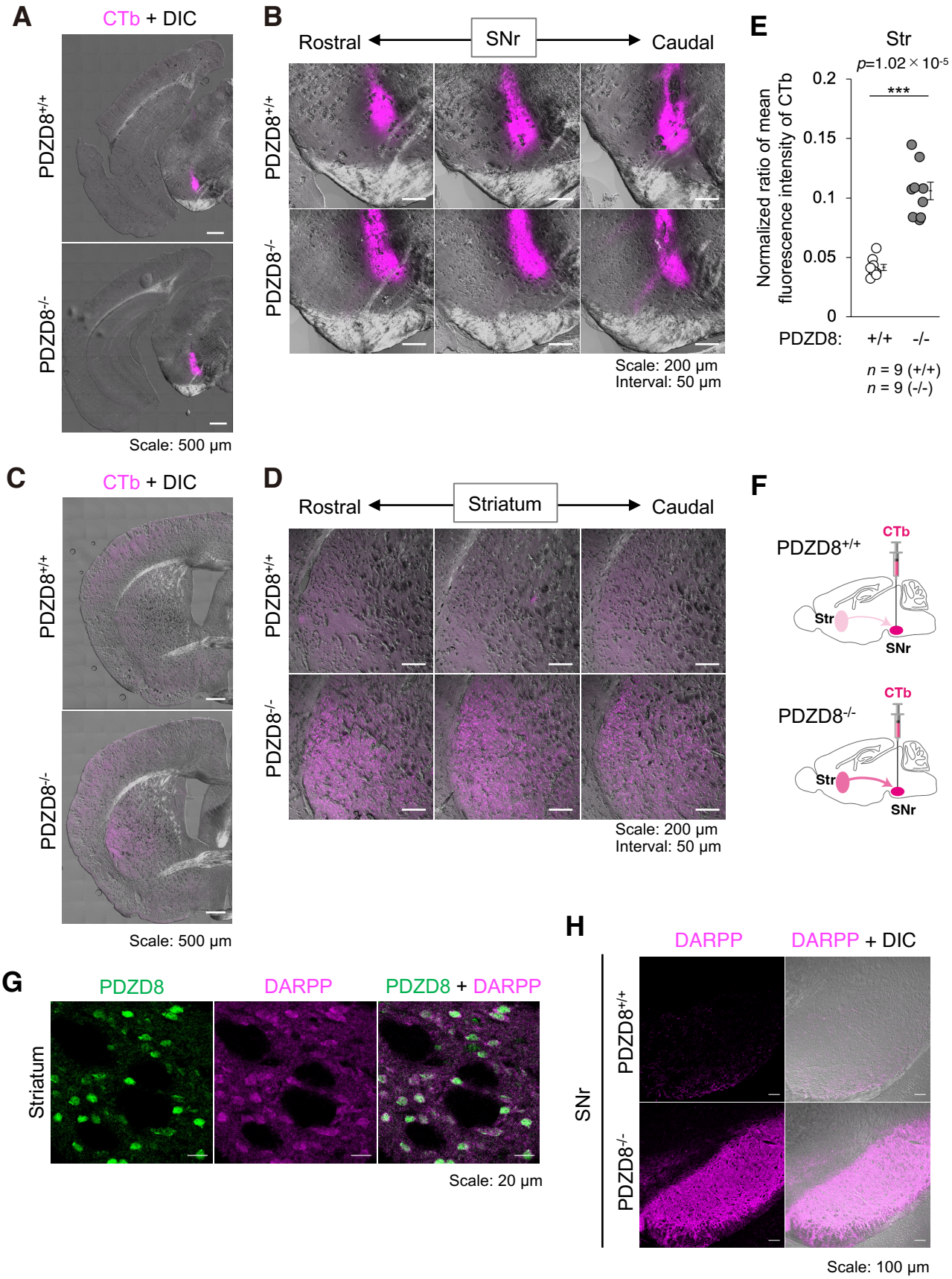
A
CTb + DIC
PDZD8+/+
PDZD8-/-
Scale: 500 μm
B
Rostral
SNr
Caudal
PDZD8+/+
PDZD8-/-
Scale: 200 μm
Interval: 50 μm
E
Str
p=1.02 × 10-5
***
Normalized ratio of mean fluorescence intensity of CTb
0.2
0.15
0.1
0.05
0
PDZD8:
+/+
-/-
n = 9 (+/+)
n = 9 (-/-)
C
CTb + DIC
PDZD8+/+
PDZD8-/-
Scale: 500 μm
D
Rostral
Striatum
Caudal
PDZD8+/+
PDZD8-/-
Scale: 200 μm
Interval: 50 μm
F
PDZD8+/+
CTb
Str
SNr
PDZD8-/-
CTb
Str
SNr
G
PDZD8
DARPP
PDZD8 + DARPP
Striatum
Scale: 20 μm
H
DARPP
DARPP + DIC
SNr
PDZD8+/+
PDZD8-/-
Scale: 100 μm

Figure 5

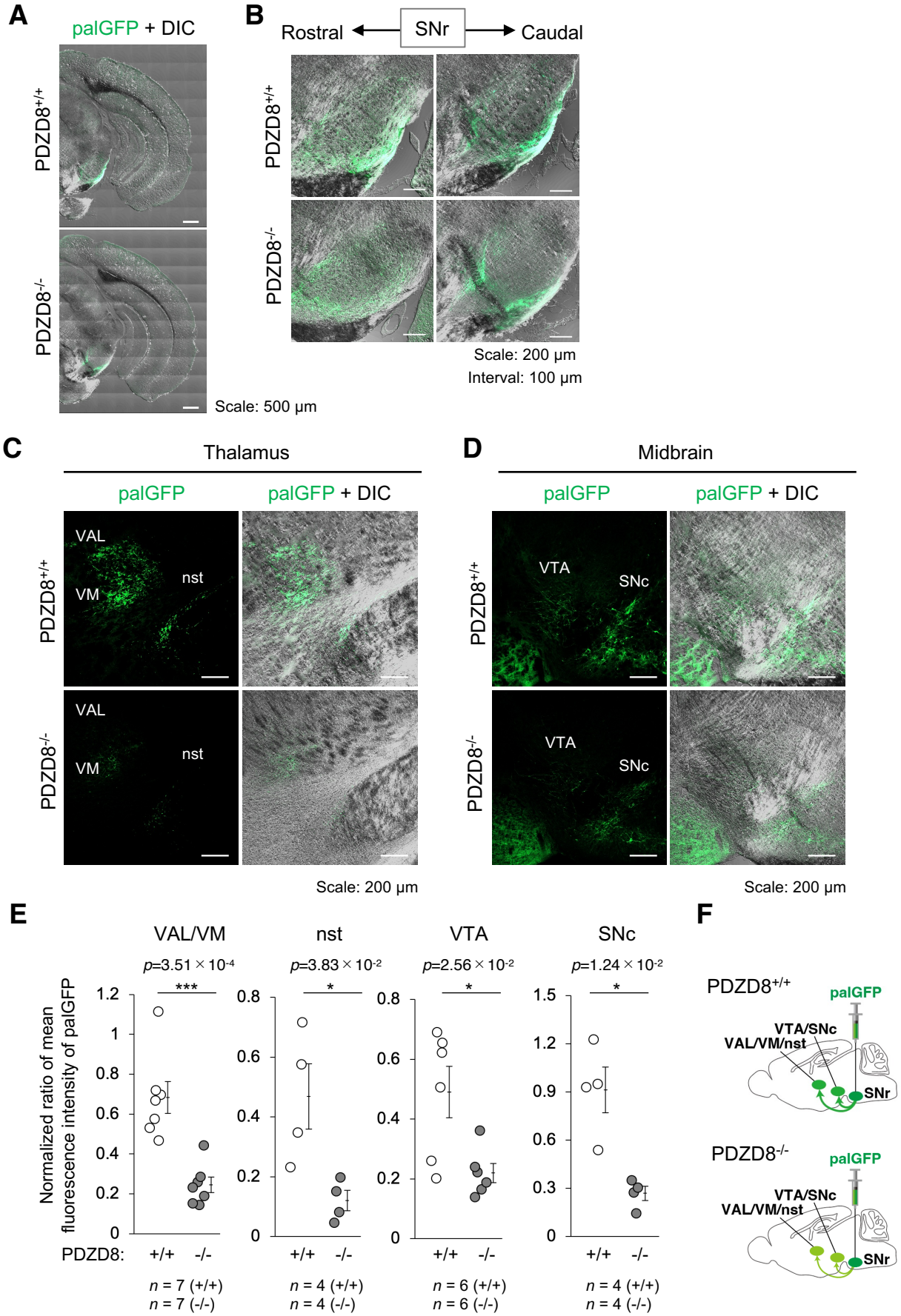
A
palGFP + DIC
PDZD8+/+
PDZD8-/-
Scale: 500 μm
B
Rostral
SNr
Caudal
PDZD8+/+
PDZD8-/-
Scale: 200 μm
Interval: 100 μm
C
Thalamus
palGFP
palGFP + DIC
VAL
VM
nst
PDZD8+/+
PDZD8-/-
Scale: 200 μm
D
Midbrain
palGFP
palGFP + DIC
VTA
SNc
PDZD8+/+
PDZD8-/-
Scale: 200 μm
E
VAL/VM
nst
VTA
SNc
p=3.51 × 10-4
p=3.83 × 10-2
p=2.56 × 10-2
p=1.24 × 10-2
***
*
*
*
Normalized ratio of mean fluorescence intensity of palGFP
PDZD8:
+/+
-/-
n = 7 (+/+)
n = 7 (-/-)
n = 4 (+/+)
n = 4 (-/-)
n = 6 (+/+)
n = 6 (-/-)
n = 4 (+/+)
n = 4 (-/-)
F
PDZD8+/+
palGFP
VTA/SNc
VAL/VM/nst
SNr
PDZD8-/-
palGFP
VTA/SNc
VAL/VM/nst
SNr

Figure 6

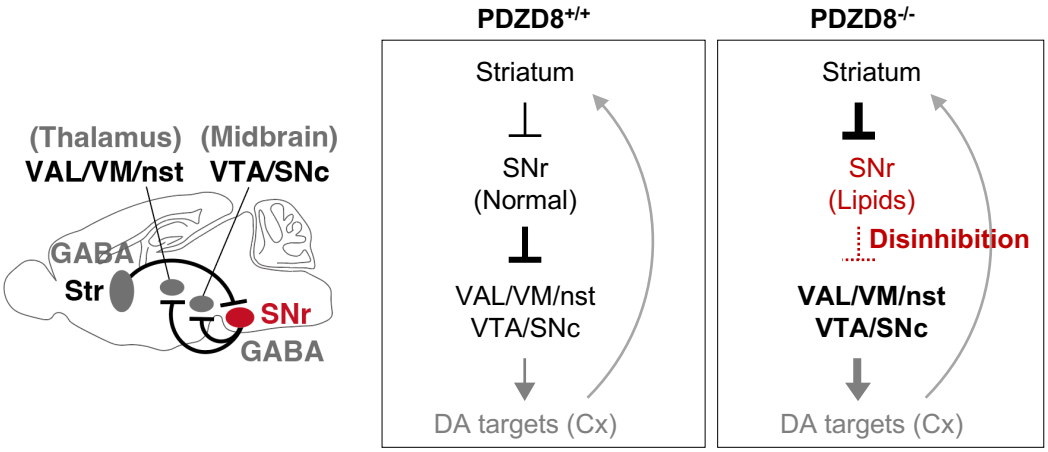
(Thalamus)
VAL/VM/nst
(Midbrain)
VTA/SNc
GABA
Str
SNr
GABA
PDZD8+/+
Striatum
SNr
(Normal)
VAL/VM/nst
VTA/SNc
DA targets (Cx)
PDZD8-/-
Striatum
SNr
(Lipids)
Disinhibition
VAL/VM/nst
VTA/SNc
DA targets (Cx)

Figure 7

A

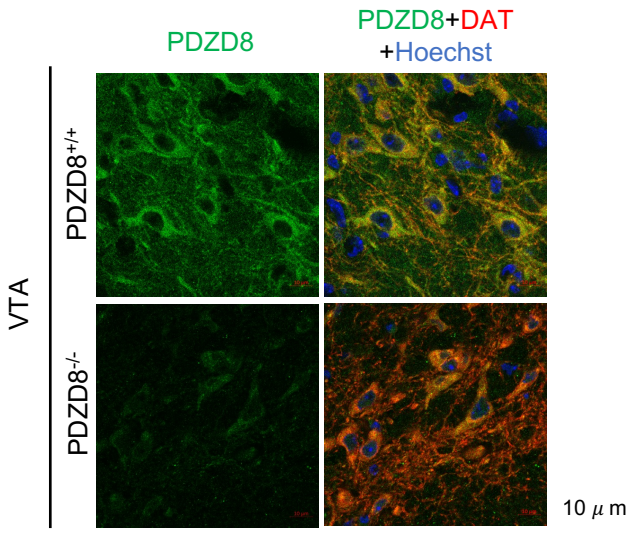

B

PDZD8 highly expressed region	NeuN (Neuron)	GFAP (Astrocyte)	Iba1 (Microglia)	TH	DAT	NET	TPH2	PV	DARPP	ChAT	CGRP	D1R	D2R
PFC	+	-		-	-		-	-	+	-		-	-
CC		+	-	-					-	-			-
Str	+	-	-	-	-	-	-	+	+	+		-	-
NAc	+	-		-	-				-			-	-
Hippo	+							+	-	-			
MHb	+	-						-	-	+			
BLA	+	-	-	-	-	-	-	+	+	+	-	-	
CeA	+	-	-	-	-	-	-		+	+	-	-	
VTA	+	-	-	+	+			-	+				
SNc	+	-	-	+	+			-	+				
SNr	+	+	-	-	-			+	+				
DR	+						+						
LC						-		-	-	-			
PBN	+									-	+		

+	Colocalization was observed between the cell marker and PDZD8.
-	Colocalization was not observed between the cell marker and PDZD8.
	Not tested

Supplementary figure 1

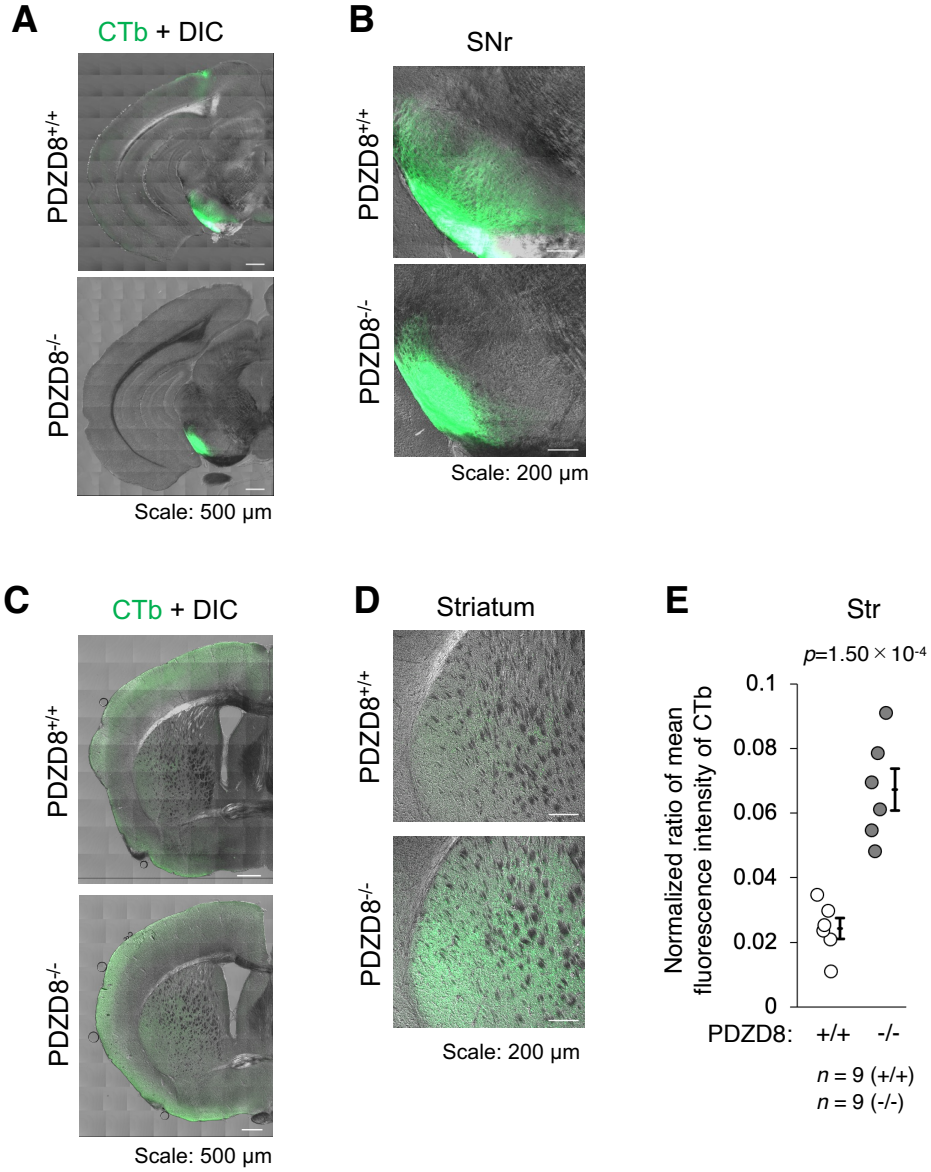

Supplementary figure 2

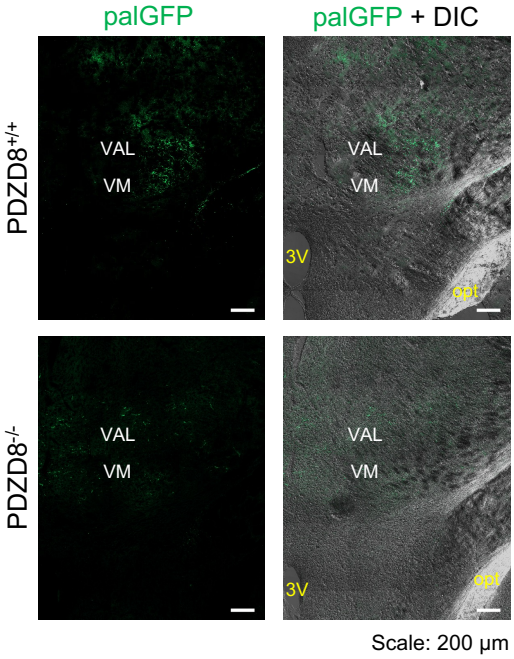

Supplementary figure 3

Information of mouse age and sex

Main figure	Age (month)	Sex (M/F)
1A	4	M
1B	6	F
1C	5	F
1D	5	F
1E	4	M
2A	7	F
2B	7	F
2C	7	F
2D	9	F
3A-C	9	M
4B, C	9	M
5A-E	4	F
5G-H	8	F
6A-E	4	M

Supplement	Age (month)	M/F
S1	8	F
S2A, B	6	F
S3A, B	4	M
Smov A, B	9	M

Supplementary table 1

Information of neuronal tracer injection

Alexa594-CTb

Concentration	2 μg/μL
Volume	200 nL
Target region	SNr
Coordinates from Bregma	AP: -3.2 mm, ML: ±1.4 mm, DV: -4.4 mm

Alexa 488-CTb

Concentration	2 μg/μL
Volume	150 nL
Target region	SNr
Coordinates from Bregma	AP: -3.7 mm, ML: ±1.8 mm, DV: -4.5 mm

AAV2/1-CMV-paIGFP

Viral titer	3.5×10^{12} vg/mL
Volume	100 nL
Target region	SNr
Coordinates from Bregma	AP: -3.7 mm, ML: ±1.8 mm, DV: -4.5 mm

Supplementary table 2